Clays and Clay Minerals (2024), **72**, e12, 1–11
doi:10.1017/cmn.2024.19

Original Paper

High catalytic performance of thermally treated Mn-rich limonite for catalytic oxidation of toluene

Shiwei Dong[1,2], Tianhu Chen[1,2], Yinsheng Zhang[1,2], Haibo Liu[1,2], Minghao Ji[1,2], Chengzhu Zhu[1,2] and Xuehua Zou[1,2]

[1]Laboratory for Nano-minerals and Environmental Materials, School of Resources and Environmental Engineering, Hefei University of Technology, Hefei 230009, China and [2]Key Laboratory of Nano-minerals and Pollution Control of Anhui Higher Education Institutes, Hefei University of Technology, Hefei 230009, China

Abstract

The development of active and low-cost transition metal oxide-based catalysts was vital for the catalytic oxidation of toluene. This study aimed to prepare Fe-Mn oxide catalysts by Mn-rich limonite, and investigate the catalytic activity and mechanism for toluene oxidation. The natural Mn-rich limonite was thermally activated at different temperatures and these thermally activated samples exhibited different oxidation activities. YL-300, obtained through thermal treatment at 300°C, exhibited excellent catalytic activity, showing 90% toluene conversion at 239°C (1000 ppm toluene) and remarkable catalytic stability even in the presence of water vapor (5 vol.%). The amount of oxygen vacancies in the catalyst was regulated by tuning the thermal treatment temperatures. Optimal thermal treatment facilitated the increase of oxygen vacancies and enhanced the oxygen mobility and redox capacity of YL-300, contributing to the complete oxidation of toluene to H_2O and CO_2. The oxidation of toluene was greatly influenced by the adsorbed oxygen species. This study demonstrates the potential of Mn-rich limonite as a promising catalyst for toluene oxidation, thereby promoting the utilization of natural mineral materials in the field of environmental pollution control.

Keywords: Fe-Mn oxides; Mn-rich limonite; thermal treatment; toluene catalytic oxidation; volatile organic compounds

(Received: 07 February 2024; revised: 20 April 2024; accepted: 26 April 2024)

Introduction

Volatile organic compounds (VOCs) could be emitted from various sources, including industrial processes, construction materials, consumer products, and furniture (Jeong et al., 2017; Dong et al., 2019). Fugitive emissions of VOCs would cause damage to human health and the eco-environment (Pöschl and Shiraiwa, 2015; Kamal et al., 2016; Ismail et al., 2023). The efficient control of VOC emissions is of great importance in maintaining a clean and healthy air environment. Over recent decades, many control technologies have been developed to diminish the emissions of VOCs, including physical adsorption, photocatalytic oxidation, plasma methods, catalytic oxidation, and others (Zhu et al., 2015; Ranjbaran et al., 2018; Mansoori et al., 2019; Deng et al., 2022; Liu et al., 2022). Of these VOC control techniques, catalytic oxidation has been recognized as the most promising method due to its high conversion efficiency, low reaction temperature, and environmentally friendly degradation characteristics (Liang et al., 2019; Rochard et al., 2021; Kim et al., 2022; Dong et al., 2023).

The core of catalytic oxidation depends on the development of efficient catalysts. To date, the catalysts used for VOC oxidation are mainly divided into noble metal-supported catalysts and metal oxide-based catalysts. Although noble-metal catalysts (e.g. Pt, Au, and Rh) have exhibited excellent catalytic performance in VOC oxidation at low temperatures, their wide applications are limited by their high cost, poor resources, and easy poisoning (Gaálová et al., 2019; Zhang et al., 2022). In comparison, transition metal oxide (TMO) catalysts (e.g. NiO, FeO_x, CoO_x, and MnO_x) have been studied extensively and show comparatively high catalytic activity for VOC elimination (Liu et al., 2020; Ilieva et al., 2021; Wang et al., 2021a; Yadav et al., 2022). To improve the catalytic performance further, mixed metal oxide catalysts (e.g. Cu-Co, Fe-Mn, and Fe-Ni) were investigated, which exhibited better catalytic activity compared with mono-metallic oxide catalysts (Carrillo and Carriazo, 2015; Chen et al., 2017; Wang et al., 2021b). Among them, Fe-Mn oxide catalysts have attracted much research attention owing to their adsorptive capacity, excellent redox properties, and sintering resistance (Lashanizadegan et al., 2021; Shah et al., 2023), showing outstanding catalytic activity and stability in VOC oxidation (Wang et al., 2018; Liu et al., 2023). These materials demonstrated great efficiency in VOC removal; however, the synthesis process was relatively complex and expensive to prepare in many cases.

Recently, natural mineral materials have gained attention as catalysts or supports in the field of environmental pollution treatment, due to their low cost, distinct structures, and physicochemical properties (Ardakani et al., 2019; Rezaei et al.,

Corresponding author: Xuehua Zou; Email: zouxuehua1988@hfut.edu.cn
Cite this article: Dong S., Chen T., Zhang Y., Liu H., Ji M., Zhu C., & Zou X. (2024). High catalytic performance of thermally treated Mn-rich limonite for catalytic oxidation of toluene. *Clays and Clay Minerals* **72**, e12, 1–11. https://doi.org/10.1017/cmn.2024.19

2019; Miao et al., 2022; Miao et al., 2023). Limonite is a mineral with nanostructure and relatively high specific surface area, showing great application prospects in environmental pollution control (Tsubouchi et al., 2015; Sahin et al., 2016). For example, mechanically activated limonite exhibited excellent efficacy for the adsorption and stabilization of As in soil (Yan et al., 2020), and the limonite was also proved to be a catalyst with great efficiency for methylene blue removal in the Fenton system (Toda et al., 2014). Compared with the removal of heavy metals and organic pollutants in water or soil environments, the treatment of gaseous containments by limonite has been rarely studied. A previous study has shown that the Fe-Mn binary oxides prepared by thermal treatment of natural Mn-rich limonite displayed excellent performance for NO reduction in a reaction temperature range of 130–300°C, due to the large specific surface area and high redox ability (Zhang et al., 2018). In fact, these properties of Fe-Mn binary oxides might also be beneficial for the removal of VOCs. On the other hand, keeping in mind the need for catalysts with high activity, which are environmentally friendly, and economic for real-world VOC removal, the preparation of Fe-Mn binary oxides by thermal activation of natural Mn-rich limonite might be a good approach.

In this study, the Fe-Mn binary oxides were prepared by thermal treatment of Mn-rich limonite at different reaction temperatures and investigated for their catalytic activity in the oxidation of toluene. The effect of different calcination temperatures on the catalytic performance of the catalysts was investigated, and the reaction mechanism of toluene oxidation over the thermally treated Mn-rich limonite is discussed. The aims of this work are to (i) explore the feasibility of the thermally treated Mn-rich limonite for toluene oxidation; (ii) to understand the kinetics and mechanism of toluene oxidation over the catalysts; and (iii) to promote the application of the natural Mn-rich limonite in VOC removal. This work provides a reference for the development of low-cost and efficient mineral-based materials for the elimination of VOCs.

Materials and methods

Preparation of catalyst

The catalysts were prepared through the thermal treatment of Mn-rich limonite at different temperatures under air atmosphere (denoted as YL-X, X=300, 400, 500, and 600, respectively). YL-Raw represents the natural Mn-rich limonite. The detailed preparation of the catalysts is shown in the Supplementary material.

Catalyst characterization

The different catalysts were characterized by X-ray diffraction (XRD), X-ray fluorescence (XRF) analysis, Raman spectroscopy, H_2 temperature-programmed reduction (H_2-TPR), O_2 temperature-programmed desorption (O-TPD), spin-trapping electron paramagnetic resonance (EPR), transmission electron microscopy (TEM), Brunauer-Emmett-Teller analysis (BET), X-ray photoelectron spectroscopy (XPS), and *in situ* diffuse reflectance infrared Fourier transform spectroscopy (*in situ* DRIFTS). The Supplementary material gives the details of the characterization.

Catalytic activity measurements

The catalytic activity of toluene oxidation was performed in a continuous-flow fixed-bed reactor (Fig. S1 in the Supplementary material). In addition, toluene conversion (η, %) and CO_2 yield (Y_{CO2}, %) were used to evaluate the catalytic activity of the catalyst. Details of the catalytic performance evaluation tests are shown in the Supplementary material.

Results and Discussion

Catalytic performance

The catalytic activity for toluene oxidation of the catalysts was measured as a function of reaction temperature (Fig. 1). The reaction temperatures corresponding to 50% and 90% toluene conversion (T_{50} and T_{90}) were used to evaluate the catalytic activity. Experimental measurements of catalytic activity (Fig. 1a) revealed that toluene conversion increased with an increase in reaction temperature, and the catalysts showed different catalytic activities in toluene oxidation. YL-Raw reached T_{50} and T_{90} values at 224 and 247°C, respectively. The catalytic activity of the catalysts changed significantly after thermal treatment; YL-300 showed the highest catalytic activity.

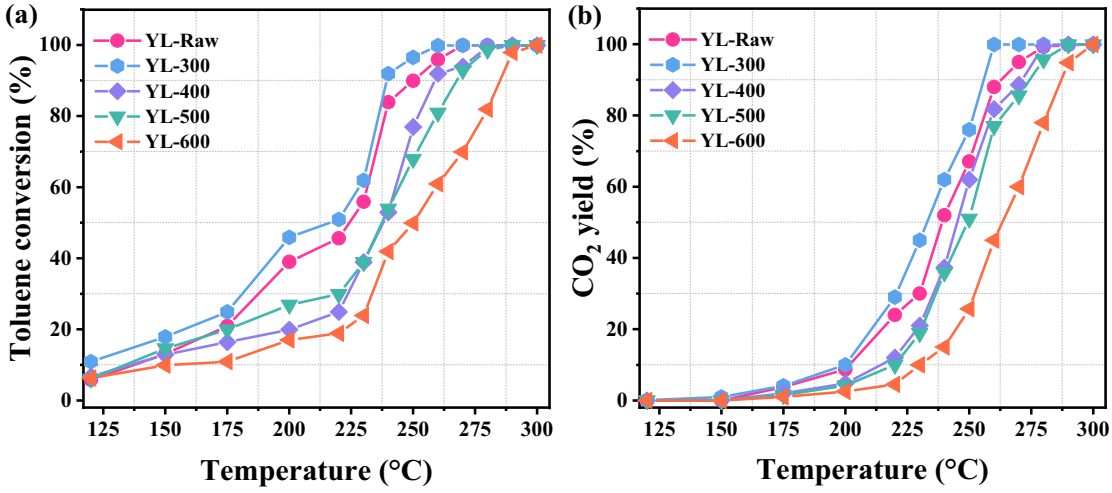

Figure 1. (a) Toluene conversion, and (b) CO_2 yield of the catalysts for toluene oxidation at different temperatures. Reaction conditions: 0.4 g catalyst, toluene 1000 ppm, total flow rate = 100 mL min^{-1}, weight hourly space velocity (WHSV) = 15,000 mL g^{-1} h^{-1}.

https://doi.org/10.1017/cmn.2024.19 Published online by Cambridge University Press

The T_{50} and T_{90} values for YL-300 were 215 and 239°C, respectively, which were lower than those of the other catalysts. In addition, the catalytic activities of Fe_2O_3 and MnO_2 (Fig. S2 in the Supplementary material) were also lower than that of YL-300. According to the values of T_{90} for toluene conversion, the catalytic activities of the catalysts were as follows: YL-600 (283°C) < YL-500 (267°C) < YL-400 (258°C) < YL-Raw (247°C) < YL-300 (239°C). The catalytic activities of the catalysts (Fig. 1a) gradually decreased as the thermal treatment temperature increased, indicating that proper thermal treatment has a positive effect on the toluene oxidation of the Mn-rich limonite catalyst.

Similar to the overall trend of toluene conversion, CO_2 yield (Fig. 1b) showed an increase with the increasing reaction temperature over the catalysts. CO_2 yield tests (Fig. 1b) revealed that YL-300 had superior catalytic activity in converting toluene to CO_2 compared with the other catalysts, achieving complete oxidation of toluene to CO_2 at 260°C. The T_{90} values of CO_2 decreased in the sequence of YL-300 > YL-Raw > YL-400 > YL-500 > YL-600. It should be noted that the CO_2 yield was lower than that of the toluene conversion at the same reaction temperature due to the incomplete conversion of the intermediate species (Chen et al., 2017). Compared with the previously reported performances of the catalysts (Table 1), YL-300 also had a higher specific reaction rate and toluene conversion under similar reaction conditions, suggesting that Mn-rich limonite has great potential for the removal of VOCs.

Catalytic stability tests

Considering the practical applications, the catalytic stability of YL-300 was evaluated at 215°C (50% toluene conversion) and 239°C (90% toluene conversion), respectively. During the long-term stability experiment over 30 h (Fig. 2a), the toluene conversion of YL-300 at 215 and 239°C remained at 50 and 90%, respectively. Reusability tests (Fig. S3 in the Supplementary material) showed that YL-300 exhibited T_{50} and T_{90} values at 215 and 240°C after three runs. The effect of WHSV on the catalytic activity of YL-300 (Fig. S4a in the Supplementary material) showed that total toluene oxidation was achieved below 260°C even at 60,000 mL g^{-1} h^{-1}). The toluene concentration effects test (Fig. S4b in the Supplementary material) showed that the temperature for total toluene oxidation at 1600 ppm was only about 10°C greater than that at 600 ppm. Catalytic stability tests (Fig. 2a; Figs S3 and S4 in the Supplementary material) confirmed the excellent catalytic stability of YL-300 for toluene oxidation further.

Table 1. Catalytic activity parameters reported on toluene over different catalysts

Catalysts	Concentration (ppm)	WHSV (mL g^{-1} h^{-1})	T_{90} (°C)	Specific reaction rate (mol s^{-1} m^{-2})	References
$30MnO–50CeO_2$	1000	—	>250	3.10×10^{-8} (315°C)	Saqer et al. (2011)
$B–MnO_2{\cdot}Co_3O_4$	1000	40,000	339	2.91×10^{-8} (330°C)	Rastegarpanah et al. (2023)
$\delta–MnO_2$	1000	60,000	245	$<2\times10^{-8}$ (200°C)	Yang et al. (2020)
$La_{0.7}Sr_{0.3}Co_{0.8}Fe_{0.2}O_3$	500	—	>250	2.26×10^{-9} (220°C)	Rousseau et al. (2009)
$6.55\%Au/Fe_2O_3$	1000	15,000	260	6.08×10^{-9} (200°C)	Han et al. (2014)
$Co_3O_4–P$	1000	15,000	241	3.2×10^{-8} (210°C)	Li et al. (2018)
$La_{0.95}Ag_{0.05}CoO_3$	1000	30,000	268	4.19×10^{-9} (225°C)	Chen et al. (2019)
YL–300	1000	20,000	239	4.12×10^{-8} (200°C)	This study

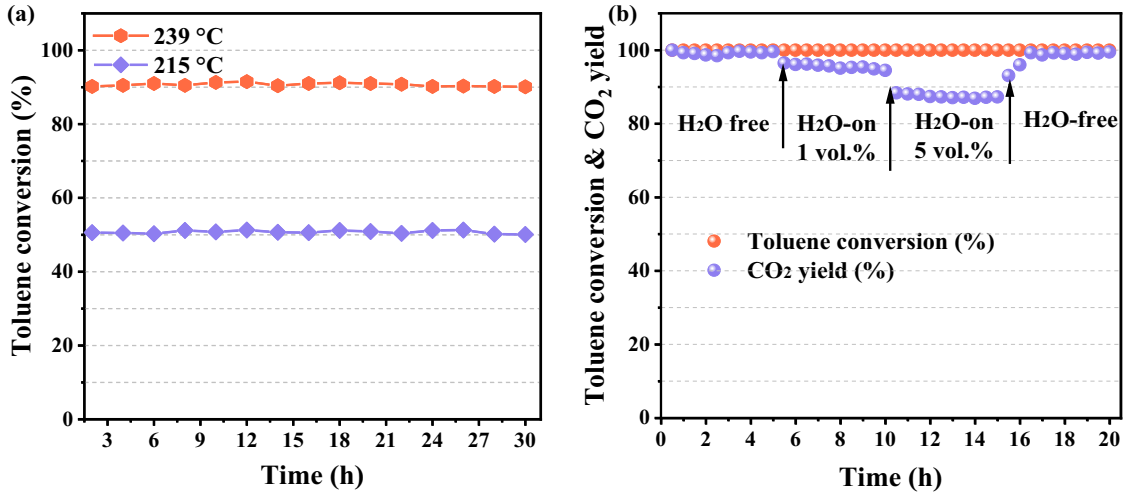

Figure 2. Stability tests of toluene oxidation over the YL-300 catalyst: (a) long-term toluene oxidation at 215 and 239°C, and (b) water-tolerant test under different humid conditions for toluene oxidation at 260°C. Reaction conditions: catalyst weight 0.4 g, toluene 1000 ppm, total flow rate = 100 mL min^{-1}, WHSV = 15,000 mL g^{-1} h^{-1}, and 21% O_2/N_2 balance gas.

https://doi.org/10.1017/cmn.2024.19 Published online by Cambridge University Press

Taking into account that the water vapor in the actual exhaust gas would compete with the reactants during the adsorption process, different concentrations of water vapor were introduced into the reaction system to probe the effect of water vapor on the catalytic performance of YL-300 at 260°C. Water vapor tests (Fig. 2b) showed that the toluene conversion of YL-300 remained unchanged at 100% after reaction for 5 h in the presence of 1 and 5 vol.% of water vapor; however, the CO_2 yield gradually decreased to 87% with the increase in water vapor from 1 to 5%. Water vapor tests (Fig. 2b) indicated that the existence of water vapor had a minimal effect on the toluene conversion to intermediate species within a certain range, but inhibited the complete conversion of intermediates (e.g. benzoate species) to CO_2 (Liu et al., 2019). The curves as a function of temperature under different water vapor conditions (Fig. S5 in the Supplementary material) showed that the water vapor had almost no effect on the toluene oxidation over YL-300, indicating the excellent property of YL-300 in water resistance. CO_2 yield could rapidly return to the initial level after ceasing the introduction of water vapor, suggesting that the influence of water vapor could be completely reversible.

Kinetic measurements

To compare the catalytic activity of the catalysts for toluene oxidation, kinetic measurements were performed in the absence of external and internal diffusion limitations (Fig. S6 in the Supplementary material). The specific reaction rate and apparent activation energy (E_a, kJ mol^{-1}) for toluene oxidation was calculated using the following equations:

$$r = \frac{C_{C_7H_8} \times Y_{CO_2} \times F}{m \times S_{BET}} \quad (1)$$

$$\ln r = -\frac{E_a}{RT} + C \quad (2)$$

where r (mol s^{-1} m^{-2}) is the specific reaction rate normalized by specific surface area, F (mL min^{-1}) is the total flow rate, Y_{CO_2} (%) corresponds to the conversion of toluene based on CO_2 generation, C_{C7H8} (ppm) denotes the toluene inlet concentration in the mixed gases, m (g) is the catalyst weight, S_{BET} (m^2 g^{-1}) is the specific surface area of the catalyst, T is the reaction temperature, and R represents the gas constant.

Specific reaction rate tests at 200°C (Fig. 3a) showed that YL-300 had the greatest toluene oxidation rate of 4.12×10^{-8} mol s^{-1} m^{-2}, which was 1.25 and 1.83 times greater than that of YL-Raw (3.29×10^{-8} mol s^{-1} m^{-2}) and YL-500 (2.25×10^{-8} mol s^{-1} m^{-2}), respectively. Apparent activation energy tests for toluene oxidation (Fig. 3b) revealed that the E_a (Fig. 3b) of YL-300 (40.4 kJ mol^{-1}) was lower than that of YL-Raw (46.8 kJ mol^{-1}) and YL-500 (50.8 kJ mol^{-1}), which was consistent with the catalytic activity (Fig. 1). Kinetic measurements (Fig. 3) further demonstrated that an appropriate thermal treatment temperature for YL could effectively improve its catalytic activity for toluene oxidation.

Catalyst characterizations

Structural and crystal properties

The structural properties of the catalysts were identified by XRD analysis. The characteristic reflections observed at 21.3, 36.6, and 53.6°2θ for YL-Raw (Fig. 4a) corresponded to the crystal faces of (110), (111), and (221) in goethite (α-FeOOH, JCPDS-81-463) (Chen et al., 2018). The peaks located at 20.8, 26.6, 50.2, 59.9, and 68.2°2θ were assigned to quartz (JCPDS-85-795), further demonstrating that YL-Raw was mainly composed of goethite and quartz. No peaks of MnO_x were found in the XRD patterns of YL-Raw, indicating that the MnO_x in YL-Raw was amorphous or poorly crystallized (Mane et al., 2023). After thermal treatment at 300°C, some new diffraction peaks corresponding to hematite (α-Fe_2O_3, JCPDS-2-915) were observed in YL-300, which were attributed to the transformation of α-FeOOH into α-Fe_2O_3 through the dehydroxylation process (González et al., 2000). Compared with YL-300, the intensities of α-Fe_2O_3 increased in the cases of YL-400, YL-500, and YL-600, while the increase in crystallinity might be related to the decrease in catalytic activity.

Raman vibration spectra of YL-Raw (Fig. 4b) showed four peaks located at about 298, 498, 557, and 664 cm^{-1} were associated with the symmetric and asymmetric stretching vibration modes of Fe-OH or Fe-O in α-FeOOH, respectively (Thibeau et al., 1978; Liu et al., 2018). Two peaks were found at 405 and 219 cm^{-1} after

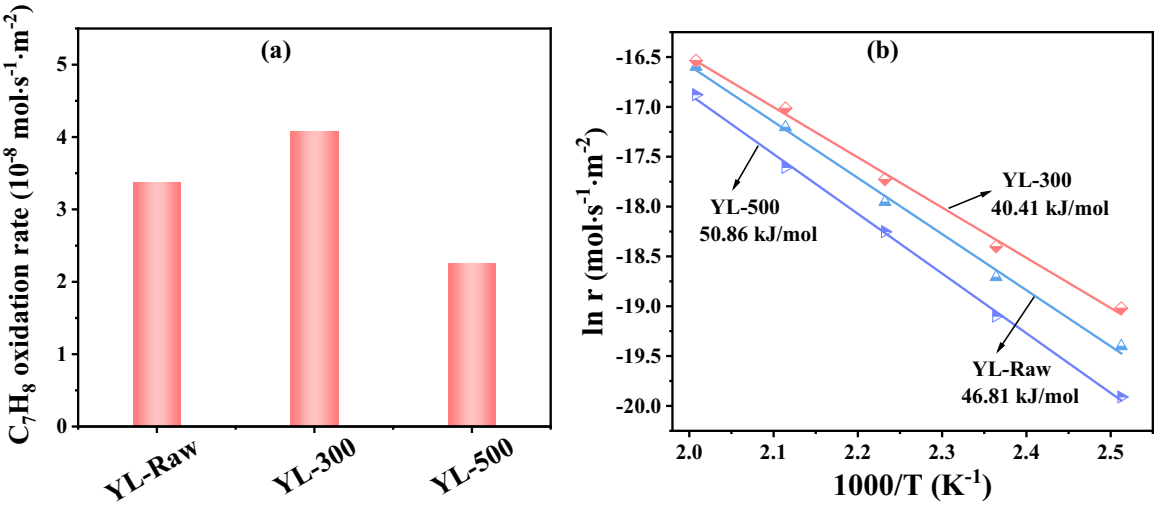

Figure 3. (a) Comparison of toluene conversion rate at 200°C; (b) Arrhenius plots of toluene oxidation over YL-Raw, YL-300, and YL-500. Reaction conditions: catalyst weight 0.15 g, toluene 1000 ppm, total flow rate = 100 mL min^{-1}, WHSV = 40,000 mL g^{-1} h^{-1}, and 21% O_2/N_2 balance gas.

https://doi.org/10.1017/cmn.2024.19 Published online by Cambridge University Press

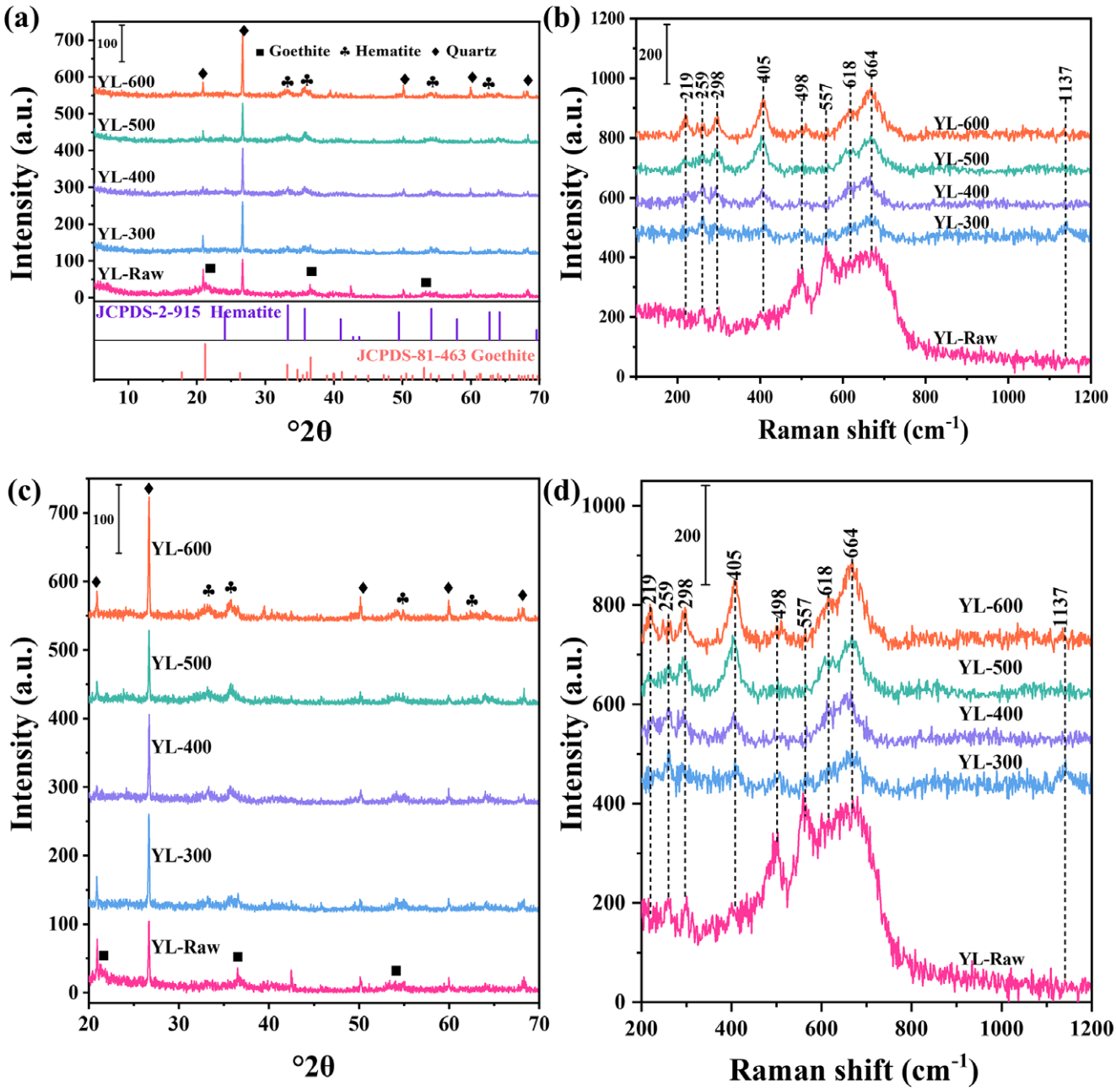

Figure 4. (a) XRD patterns and (b) Raman spectra, and (c) enlarged section of the XRD patterns and (d) Raman spectra of the catalysts.

thermal treatment, which were assigned to the E_g and A_{1g} vibrations of the Fe-O bond in α-Fe_2O_3 (Oh et al., 1998). Two peaks related to the stretching vibrations of the Mn-O bond within the octahedron structure were observed at 259 and 618 cm^{-1} (White and Keramidas, 1972). The Raman spectral band at 1137 cm^{-1} was related to the oxygen vacancies in the metal oxide catalysts (Spanier et al., 2001). Raman tests (Fig. 4b) revealed that YL-300 had a distinct peak at 1137 cm^{-1}, indicating that an appropriate thermal treatment temperature was favorable for the formation of oxygen vacancies. The presence of oxygen vacancies facilitated the replenishment and activation of gas-phase oxygen and promoted the toluene oxidation activity, which was consistent with the catalytic activity of the catalysts (Fig. 1).

TEM images (Fig. 5) revealed the structures of the catalysts at different thermal treatment temperatures. Mn was found in EDS mapping (Fig. 5a–d) despite the phases of MnO_2 being absent in XRD patterns due to the high distribution of Mn in limonite or the detection limit of XRD (Fig. 5b,c).

TEM images of YL-Raw (Fig. 5e) showed that YL-Raw had a compact needle-like structure with a diameter of around 4–8 nm. Selected area electron diffraction (SAED; Fig. 5f) and HRTEM (Fig. 5g) revealed that the YL-Raw sample consisted mainly of compact needle-like α-FeOOH and MnO_2. The structure of YL-300 (Fig. 5h) became loose after calcination at 300°C, but still maintained the needle-like structure. Also, the specific surface area increased from 96.9 $m^2 g^{-1}$ (YL-Raw) to 115.8 $m^2 g^{-1}$ (YL-300) after

https://doi.org/10.1017/cmn.2024.19 Published online by Cambridge University Press

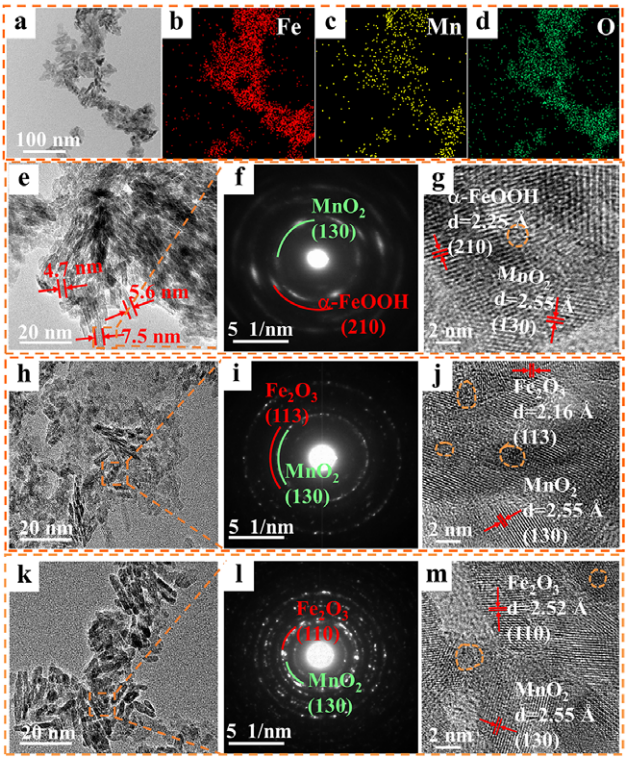

Figure 5. Elemental mapping images of YL-Raw (a–d). TEM and HRTEM images of YL-Raw (e,g), YL-300 (h,j), and YL-500 (k,m). Selected area electron diffraction patterns of YL-Raw (f), YL-300 (i), and YL-500 (l).

calcination at 300°C. The crystal plane of α-Fe_2O_3 found in YL-300 (Fig. 5i,j) showed that α-FeOOH particles were transformed into α-Fe_2O_3 after thermal treatment. The structure of YL-500 particles remained unchanged after further calcination at 500°C (Fig. 5k), and the plane of α-Fe_2O_3 was also observed (Fig. 5l,m). The specific surface area of YL-500 (80.6 m^2 g^{-1}) decreased compared with YL-Raw and YL-300 due to the sintering of the particles at high calcination temperatures. Some defect pits with irregular lattice spacing (marked with orange dashed lines in Fig. 5g,j,m) were found in the samples, which might be associated with oxygen vacancies generated on the surface of α-FeOOH (Liu et al., 2018; Cao et al., 2019). Defect sites served as active reaction centers, facilitating the transformation of gas-phase oxygen into reactive oxygen species and thus increasing the toluene oxidation reaction rate (Yang et al., 2020).

Surface properties

The surface chemical environment on the surfaces of the catalysts was investigated, and the ratios of Fe, Mn, and O species were calculated by their integrated areas (Fig. 6). The Fe $2p_{3/2}$ spectrum (Fig. 6a) showed two distinct peaks centered at about 710.5 and 712.5 eV, corresponding to Fe^{2+} and Fe^{3+} on the surface of the catalysts, respectively (Liang et al., 2022). The surface content ratio of $Fe^{3+}/(Fe^{2+}+Fe^{3+})$ of the catalysts decreased in the order of YL-300 (62.2%) > YL-Raw (59.1%) > YL-500 (53.6%). Previous studies have proved that a greater concentration of Fe^{3+} could improve the catalytic performance of the catalysts in the low-temperature oxidation of VOCs (Xue et al., 2020). The Mn $2p_{3/2}$ spectra (Fig. 6b) of the catalysts were classified into three peaks:

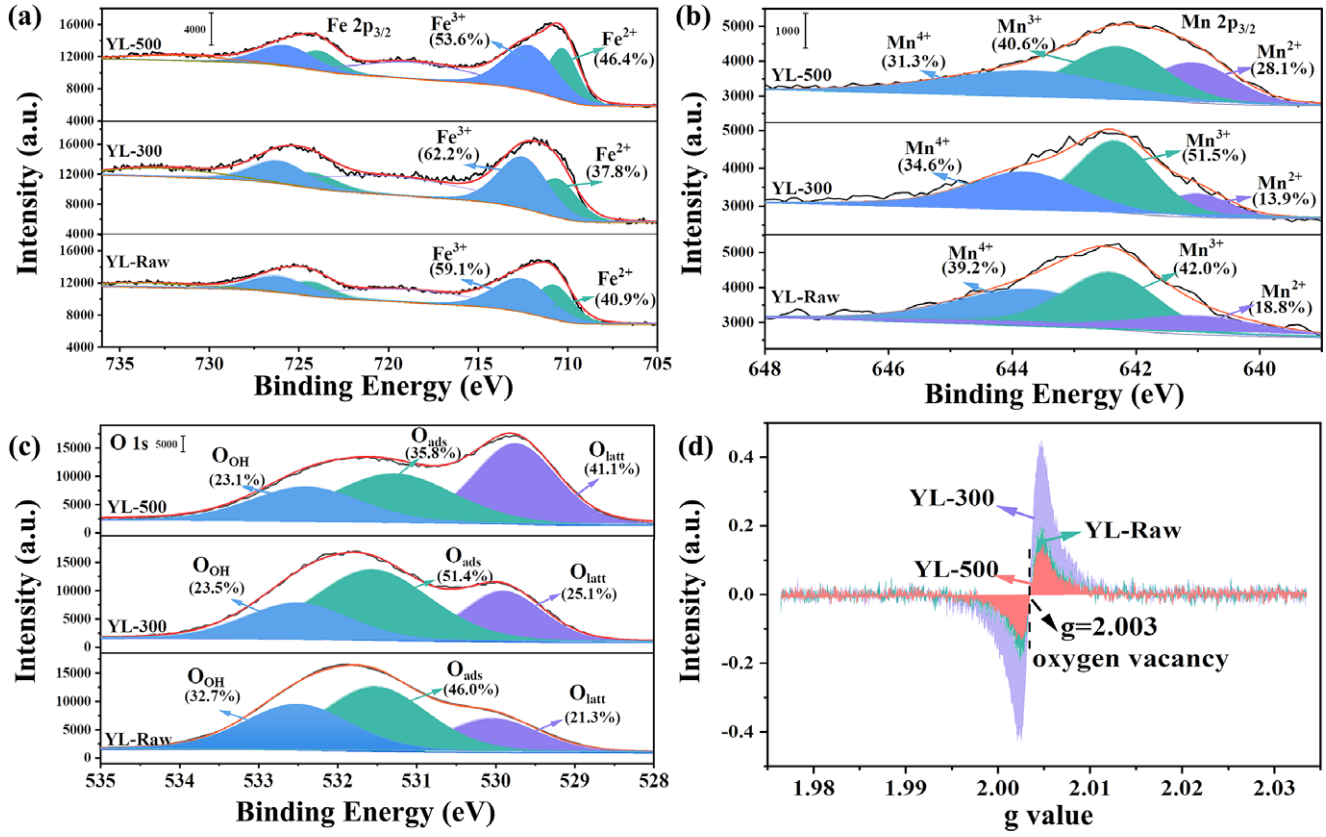

Figure 6. (a) Fe-$2p_{3/2}$, (b) Mn-$2p_{3/2}$, and (c) O 1s of the XPS spectra and (d) EPR profiles of YL-Raw, YL-300, and YL-500.

https://doi.org/10.1017/cmn.2024.19 Published online by Cambridge University Press

Mn^{2+} (641.0 eV), Mn^{3+} (642.4 eV), and Mn^{4+} (643.7 eV) (Zhang et al., 2018). The formation of Mn^{3+} in the catalyst could facilitate the dissociation and activation of oxygen atoms and the generation of oxygen vacancies. More Mn^{3+} led to more oxygen vacancies and improved the catalytic performance for the oxidation of VOCs (Hong et al., 2019; Yang et al., 2020). YL-300 had the greatest ratio of Mn^{3+} (51.5%) compared with that of YL-Raw (42.0%) and YL-500 (40.6%), which was consistent with the catalytic performance in Fig. 1.

Figure 6c shows three distinct peaks at around 529.9, 531.5, and 532.5 eV, which correspond to the lattice oxygen (O_{latt}), surface adsorbed oxygen (O_{ads}), and surface hydroxyl species (O_{OH}), respectively (Patterson et al., 1976). In general, the amount of O_{ads} represents the amount of surface oxygen vacancies on the catalyst surface and plays an important role in promoting the deep oxidation of VOCs (Hong et al., 2019). The ratio of O_{ads}/O_{total} decreased in the order YL-300 (51.4%) > YL-Raw (46.0%) > YL-500 (35.8%), showing the same trend as the catalytic performance in the catalysts. The variation of O_{ads}/O_{total} (Fig. 6c) and the catalytic activity (Fig. 1) indicated that a proper thermal treatment temperature was favorable to promote the generation of surface oxygen vacancies, thus enhancing the catalytic performance of the catalysts. The amount of oxygen vacancy in the catalysts was also examined by electron paramagnetic resonance (EPR) spectroscopy (Fig. 6d). YL-300 exhibited the strongest oxygen vacancy signal at g = 2.003, which was higher than that of YL-Raw and YL-500. According to the Mars–van Krevelen mechanism, oxygen vacancies play a key role in toluene oxidation. The greater the concentration of oxygen vacancies, the easier the adsorption and activation of gas-phase oxygen to form adsorbed oxygen species (O_{ads}) on the catalyst surface. EPR test (Fig. 6d) showed that the amount of oxygen vacancies was in the order of YL-300 > YL-Raw > YL-500. XPS and EPR tests of the catalysts (Fig. 6) further indicated that the proper thermal treatment promoted the generation of surface oxygen vacancies and facilitated the mobility of the oxygen species, thus improving the catalytic activity of the catalysts for toluene oxidation.

Redox properties of the catalysts

H_2-TPR and O_2-TPD experiments were conducted to evaluate the redox behavior of the catalysts. H_2-TPR test of YL-Raw (Fig. 7) showed four peaks at 311, 340, 420, and 698°C, relating to the reduction of MnO_2 to Mn_2O_3, Mn_2O_3 to Mn_3O_4, Fe_2O_3 to Fe_3O_4, and Fe_3O_4 to FeO, respectively (Durán et al., 2009; Chen et al., 2017; Qin et al., 2019). These reduction peaks shifted to lower temperatures over YL-300 while shifting to higher temperatures over YL-500. Experimental measurements of H_2-TPR (Fig. 7) demonstrated that the thermal treatment temperature would affect the reducibility of the catalysts. The reducibility of the catalysts decreased in the order YL-300 > YL-Raw > YL-500, consistent with their catalytic performance for toluene conversion.

The O_2-TPD curve (Fig. 7b) showed three desorption regions: low (100–300°C), medium (300–550°C), and high (>550°C) temperature regions. These regions corresponded to different oxygen species: physical or chemically adsorbed oxygen species (O_I), the oxygen adsorbed on surface vacancies or surficial lattice oxygen (O_{II}), and bulk lattice oxygen species (O_{III}), respectively (Nie et al., 2017; Sun et al., 2022). The desorption peaks of YL-300 were lower than those of YL-Raw and YL-500, indicating its better oxygen migration ability, resulting in a faster reaction with adsorbed toluene on the catalyst surface. Previous studies have indicated that these oxygens of O_{II} were generally adsorbed on the sites of oxygen vacancies and participated in the reactions for the VOCs deep oxidation (Hong et al., 2019). Among these catalysts, YL-300 had the largest integrated area of O_{II} compared with YL-Raw and YL-500, thus displaying the best catalytic activity for toluene oxidation. The H_2-TPR and O_2-TPD experiments (Fig. 7) showed that the oxygen migration ability and redox capacity of the catalysts were in the order of YL-300 > YL-Raw > YL-500, indicating that an appropriate thermal treatment could promote toluene oxidation by improving the redox properties.

Relationship between catalytic activity and catalyst properties

The thermal treatment temperature showed a significant effect on the properties of the catalyst, including specific surface area, oxygen species, and oxygen vacancies. These variations would further affect the catalytic performance of toluene oxidation. YL-300 had the largest specific surface area of 115.8 $m^2\ g^{-1}$, which was higher than that of YL-Raw (96.9 $m^2\ g^{-1}$) and YL-500 (80.6 $m^2\ g^{-1}$), respectively. In general, a larger specific surface area corresponds to a lager contact area and more effective catalytic activity (Cheng et al., 2023). The presence of abundant surface oxygen vacancies could contribute to the participation of more surface-adsorbed oxygen species in the toluene oxidation reaction (Li et al., 2018). The XPS results indicated the largest ratio of O_{ads}/O_{total} over YL-300. The linear relationship (Fig. 8) between T_{90} and the specific surface area (R^2=0.86), surface O_{ads} abundance (R^2=0.98), and surface oxygen vacancy abundance (R^2=0.92) of the catalysts

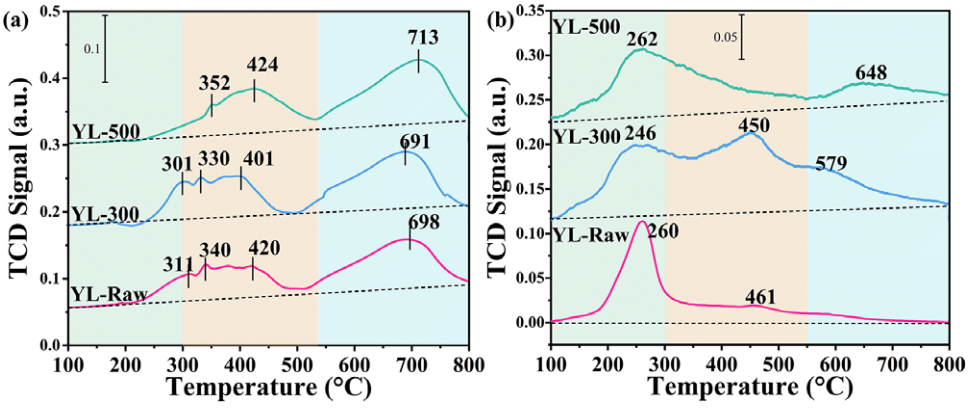

Figure 7. (a) H_2-TPR and (b) O_2-TPD profiles of YL-Raw, YL-300, and YL-500.

https://doi.org/10.1017/cmn.2024.19 Published online by Cambridge University Press

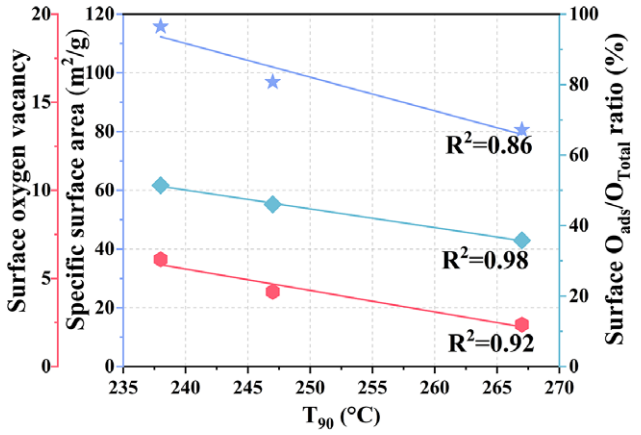

Figure 8. The relationship between T_{90} and catalyst properties.

was calculated. Therefore, the surface O_{ads} should be the most significant factor for toluene oxidation, while the specific surface area might not be the key factor for the catalytic activity.

Toluene oxidation pathway and mechanism

In situ DRIFTS was used to investigate the generated intermediates and the reaction mechanism further during the toluene oxidation over YL-300. The peaks corresponding to various intermediate species related to toluene oxidation and their attribution were summarized (see Supplementary material, Table S1).

The typical set of temperature-dependent DRIFTS spectra for toluene oxidation over YL-300 within the range of 30–260°C was performed (Fig. 9a). The surface adsorption species changed significantly with the variations of reaction temperatures. For example, a strong band appearing at 1493 cm^{-1} upon the introduction of toluene into the system at 30°C should be ascribed to the υ(C=C) vibration of the aromatic ring in toluene, demonstrating the adsorption of toluene on the surface of YL-300 (Yang et al., 2020). Two weak peaks at 1081 and 1178 cm^{-1} were associated with the stretching vibrations of υ(C-O) in benzyl alcohol (Mo et al., 2020). This indicated that the adsorbed toluene on the surface of YL-300 was further transformed into benzyl alcohol (C_6H_5-CH_2O-) species at low temperatures by the oxidation of surface oxygen species (Dong et al., 2019). The 1493 cm^{-1} band decreased significantly when the reaction temperature was increased to 120°C, while two bands at 1452 and 1594 cm^{-1} corresponding to the vibrations of the skeleton υ(C=C) in benzene ring of benzaldehyde were observed (Shen et al., 2022; Shen et al., 2023). This observation confirmed the further degradation of toluene and oxidation of benzyl alcohol groups at greater reaction temperatures. Two peaks at 1414 and 1543 cm^{-1} corresponded to the symmetric and anti-symmetric stretching vibrations of υ(C-O) in the carboxylate group, respectively, suggesting the formation of benzoate species on the catalyst surface (Shen et al., 2022). A weak peak of the maleic anhydride species appeared at 1304 cm^{-1} when the temperature reached 175°C, indicating benzyl alcohol and benzoate would be further converted into anhydride species (Tang et al., 2022).

To distinguish the change of the intermediate species during toluene oxidation, the integrated area of characteristic peaks representing the intermediates of benzyl alcohol (1178 cm^{-1}), anhydride (1304 cm^{-1}), and benzoate (1414 cm^{-1}) were evaluated (Fig. 9b). Benzyl alcohol and benzoate species accumulated on the catalyst surface at lower reaction temperatures, and then, gradually converted into anhydride species at higher temperatures. The integrated area of benzoate species reached the maximum at 200°C, while the maximum integrated area of anhydride was presented at 240°C. In general, ring opening usually demands greater reaction temperatures. It can be deduced that the further conversion of benzoate species into anhydride species should be the rate-limiting step in the oxidation of toluene. The time-dependent DRIFTS spectra of toluene oxidation over YL-300 recorded at 260°C (Fig. 9c,d) showed that the anhydride did not accumulate further as the reaction time increased, demonstrating that the intermediates were continuously oxidized into H_2O and CO_2.

To explore the effect of oxygen species, the toluene adsorption process over YL-300 was exposed to 300 ppm toluene-N_2 (Fig. 9e). The intensities of the peaks corresponding to various intermediate species and the peak areas increased with the reaction temperature under the N_2 condition (Fig. 9f). It should be noted that these peaks of different intermediates had reduced intensities under air condition than those of the peaks under N_2. The results indicated that the presence of surface lattice oxygen over YL-300 could be utilized and responsible for the oxidation of toluene to some extent, whereas these intermediates were difficult to completely oxidize into H_2O and CO_2 without the replenishment of gaseous oxygen. This was attributed to the fact that gaseous oxygen could be readily replenished on the catalyst surface and facilitated the regeneration of reactive oxygen species, thus improving the deep conversion of intermediates (Mo et al., 2020).

Based on the *in situ* DRIFTS results, the reaction mechanism for toluene oxidation over YL-300 (Fig. 10) involved the initial adsorption of toluene on the catalyst surface at low temperature, then the C-H bond of the methyl group was attacked by reactive oxygen species to generate benzyl (C_6H_5-CH_2) and benzyl alcohol (C_6H_5-CH_2O-). After that, the oxidation of benzyl alcohol continued with increasing temperature to form benzaldehyde, benzoate (C_6H_5-COO), and maleic anhydride, and finally toluene was converted into H_2O and CO_2. The rate-limiting step in toluene oxidation was determined to be the further oxidation of benzoate species accumulated on the YL-300 surface. Surface lattice oxygen in YL-300 could partially participate in toluene oxidation, but the intermediates formed during the oxidation by surface lattice oxygen species were difficult to further convert into CO_2 and H_2O. The oxygen adsorbed on the surface of YL-300 played a crucial role in toluene oxidation and could be replenished by activating the gas-phase oxygen through oxygen vacancies.

Conclusions

In this study, the Fe-Mn oxide catalysts with nanostructure were obtained successfully through the thermal treatment of natural Mn-rich limonite. The catalytic performance and reaction mechanism of the catalysts in toluene oxidation were investigated. The different thermal treatment temperatures induced the variations in specific surface areas and oxygen vacancies of the catalysts, which further affected the catalytic activities for toluene conversion. YL-300 exhibited the best catalytic activity with T_{90} (90%) value of 239°C and 100% toluene conversion at 260°C. The existence of water vapor (5 vol.%) showed negligible effect on the toluene conversion of YL-300 at 260°C. The excellent catalytic activity of YL-300 was related to its higher surface O_{ads} species and abundant oxygen vacancies. *In situ* DRIFTS results suggested that the conversion pathway for toluene oxidation over

https://doi.org/10.1017/cmn.2024.19 Published online by Cambridge University Press

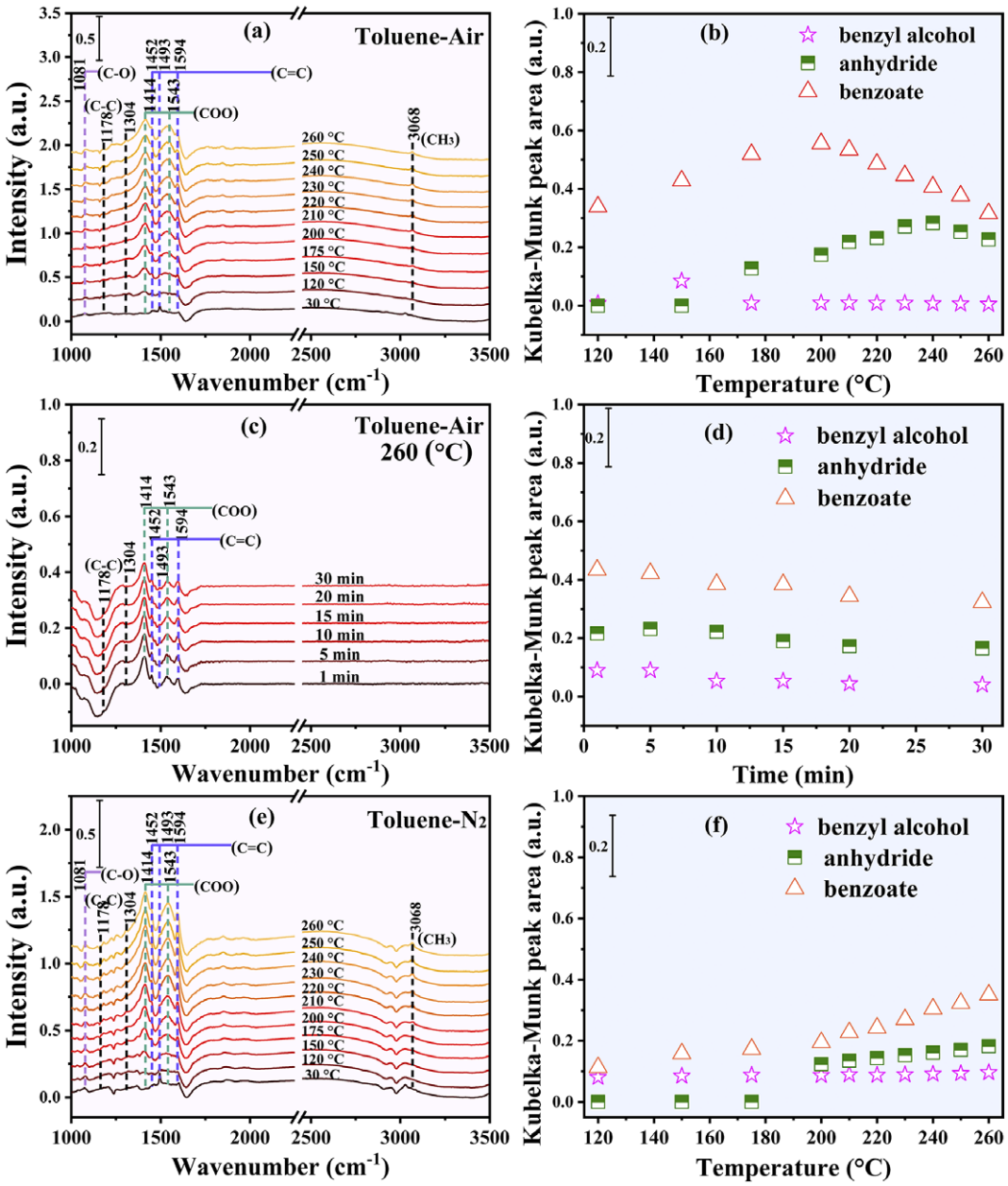

Figure 9. *In situ* DRIFTS study: (a) toluene oxidation with air, (c) toluene oxidation *vs* time at 260°C, (e) toluene oxidation with N_2; (b), (d), and (f) characteristic infrared peak areas of benzyl alcohol, benzoate, and anhydride species *vs* temperature and time for toluene oxidation.

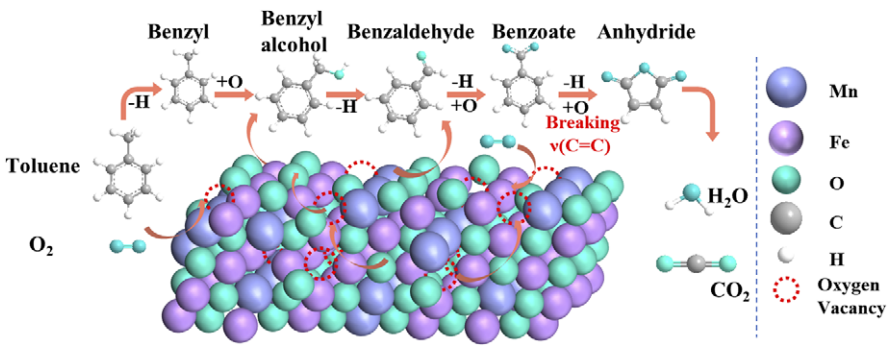

Figure 10. Schematic diagram of the proposed mechanism for the oxidation of toluene on YL-300.

https://doi.org/10.1017/cmn.2024.19 Published online by Cambridge University Press

YL-300 was: toluene → benzyl species → benzyl alcohol → benzaldehyde → benzoate species→ maleic anhydride → H_2O and CO_2. The cleavage of the C=C bond in benzoate species should be regarded as the rate-limiting step. This work provides a reference for exploring the effect of thermal treatment temperature on the properties of natural materials, thus improving the catalytic activity and promoting the application of natural materials.

Supplementary material. The supplementary material for this article can be found at http://doi.org/10.1017/cmn.2024.19.

Author contribution. All authors contributed to the study concept and design. Methodology, writing - original draft, data curation, and formal analysis were performed by Shiwei Dong. Supervision and funding acquisition were performed by Tianhu Chen. Yinsheng Zhang and Haibo Liu made the formal analysis and investigation. Minghao Ji participated in the process of formal analysis and validation. Chengzhu Zhu supported the resources. Conceptualization, writing - review & editing, and funding acquisition were performed by Xuehua Zou.

Acknowledgements. None.

Financial support. The work was supported by the National Natural Science Foundation of China (Nos. 42102029 and 41872040), the Anhui Provincial Natural Science Foundation (No. 2108085QD164), and the Fundamental Research Funds for the Central Universities (No. JZ2022HGTB0359).

Competing interest. The authors declare that they have no competing interests.

Data availability statement. Not applicable.

References

Ardakani, M.B., Mahabadi, H.A., & Jafari, A.J. (2019). Removal of toluene from air streams by cobalt-copper bimetallic catalysts supported on sepiolite. *Toxicological & Environmental Chemistry*, *101*, 228−243.

Cao, Y., Zheng, X., Du, Z., Shen, L., Zheng, Y., Au, C., & Jiang, L. (2019). Low-temperature H_2S removal from gas streams over γ-FeOOH, γ-Fe_2O_3, and α-Fe_2O_3: effects of the hydroxyl group, defect, and specific surface area. *Industrial & Engineering Chemistry Research*, *58*, 19353−19360.

Carrillo, A.M., & Carriazo, J.G. (2015). Cu and Co oxides supported on halloysite for the total oxidation of toluene. *Applied Catalysis B: Environmental*, *164*, 443−452.

Chen, H., Wei, G., Liang, X., Liu, P., He, H., Xi, Y., & Zhu, J. (2019). The distinct effects of substitution and deposition of Ag in perovskite $LaCoO_3$ on the thermally catalytic oxidation of toluene. *Applied Surface Science*, *489*, 905−912.

Chen, J., Chen, X., Xu, W., Xu, Z., Chen, J., Jia, H., & Chen, J. (2017). Hydrolysis driving redox reaction to synthesize Mn-Fe binary oxides as highly active catalysts for the removal of toluene. *Chemical Engineering Journal*, *330*, 281−293.

Chen, P., Chen., T., Xie., Q., Xu., L., Liu., H., & Zhou, Y. (2018). Mineralogy and geochemistry of limonite as a weathering product of ilvaite in the Yeshan iron deposit, Tongling, China. *Clays and Clay Minerals*, *66*, 190−207.

Cheng, G., Song, Z., Zhang, J., Qi, G., Liang, T., Cui, Q., Guo, Z., Jin, M., Li, H., Mao, L., Pang, D., & Fan, J. (2023). An investigation of the activity and mechanism of the catalytic oxidation of toluene by $FeMnO_x$ catalyst. *Molecular Catalysis*, *550*, 113573−113581.

Deng, J., Lei, W., Fu, J., Jin, H., Xu, Q., & Wang, S. (2022). Enhanced selective photooxidation of toluene to benzaldehyde over Co_3O_4-modified BiOBr/AgBr S-scheme heterojunction. *Solar RRL*, *6*, 2200279−2200288.

Dong, C., Qu, Z.P., Qin, Y., Fu, Q., Sun, H.C., & Duan, X.X. (2019). Revealing the highly catalytic performance of spinel $CoMn_2O_4$ for toluene oxidation: involvement and replenishment of oxygen species using in situ designed-TP techniques. *ACS Catalysis*, *9*, 6698−6710.

Dong, N., Chen, M., Ye, Q., Zhang, D., & Dai, H. (2023). Promotional effect of cobalt doping on catalytic performance of cryptomelane-type manganese oxide in toluene oxidation. *Journal of Environmental Sciences*, *126*, 263–274.

Durán, F.G., Barbero, B.P., Cadús, L.E., Rojas, C., Centeno, M.A., & Odriozola, J. A. (2009). Manganese and iron oxides as combustion catalysts of volatile organic compounds. *Applied Catalysis B: Environmental*, *92*, 194−201.

Gaálová, J., Topka, P., Kaluža, L., Soukup, K., & Barbier, J. (2019). Effect of gold loading on ceria-zirconia support in total oxidation of vocs. *Catalysis Today*, *333*, 190−195.

González, G., Sagarzazu, A., & Villalba, R. (2000). Study of the mechano-chemical transformation of goethite to hematite by TEM and XRD. *Materials Research Bulletin*, *35*, 2295−2308.

Han, W., Deng, J., Xie, S., Yang, H., Dai, H., & Au, C.T. (2014). Gold supported on iron oxide nanodisk as efficient catalyst for the removal of toluene. *Industrial & Engineering Chemistry Research*, *53*, 3486−3494.

Hong, W., Zhu, T., Sun, Y., Wang, H., Li, X., & Shen, F. (2019). Enhancing oxygen vacancies by introducing Na^+ into OMS-2 tunnels to promote catalytic ozone decomposition. *Environmental Science & Technology*, *53*, 13332−13343.

Ilieva, L., Petrova, P., Venezia, A.M., Anghel, E.M., State, R., Avdeev, G., & Tabakova, T. (2021). Mechanochemically prepared Co_3O_4-CeO_2 catalysts for complete benzene oxidation. *Catalysts*, *11*, 1316−1334.

Ismail, A., Zahid, M., Ali, S., Bakhtiar, S.u.H., Ali, N., Khan, A., & Zhu, Y. (2023). Engineering of oxygen vacancy defect in CeO_2 through Mn doping for toluene catalytic oxidation at low temperature. *Environmental Research*, *226*, 115860−115869.

Jeong, S.-Y., Yoon, J.-W., Kim, T.-H., Jeong, H.-M., Lee, C.-S., Chan Kang, Y., & Lee, J.-H. (2017). Ultra-selective detection of sub-ppm-level benzene using Pd–SnO_2 yolk–shell micro-reactors with a catalytic Co_3O_4 overlayer for monitoring air quality. *Journal of Materials Chemistry A*, *5*, 1446−1454.

Kamal, M.S., Razzak, S.A., & Hossain, M.M. (2016). Catalytic oxidation of volatile organic compounds (VOCs) – a review. *Atmospheric Environment*, *140*, 117−134.

Kim, S.-I., Im, M., Cho, E., Jang, H., Jang, S.Y., Kim, D.W., Kim, K.W., Heo, I., Kim, Y.J., & Lee, J.H. (2022). Effects of thermal aging on the electronic and structural properties of Pt-Pd and toluene oxidation activity. *Science of the Total Environment*, *847*, 157482−157491.

Lashanizadegan, M., Mirzazadeh, H., & Ahmadi, M. (2021). Fe-Nn-Si-O and Fe-Mn-Si-O/multi walled carbon nanotubes: synthesis, characteristics, adsorption and catalytic behavior. *Inorganic and Nano-Metal Chemistry*, *157*.

Li, G., Zhang, C., Wang, Z., Huang, H., Peng, H., & Li, X. (2018). Fabrication of mesoporous Co_3O_4 oxides by acid treatment and their catalytic performances for toluene oxidation. *Applied Catalysis A: General*, *550*, 67−76.

Liang, X., Wang, L., Wen, T., Liu, H., Zhang, J., Liu, Z., Zhu, C., & Long, C. (2022). Mesoporous poorly crystalline α-Fe_2O_3 with abundant oxygen vacancies and acid sites for ozone decomposition. *Science of the Total Environment*, *804*, 150161−150172.

Liang, Y., Liu, Y., Deng, J., Zhang, K., Hou, Z., Zhao, X., Zhang, X., Zhang, K., Wei, R., & Dai, H. (2019). Coupled palladium-tungsten bimetallic nanosheets/TiO_2 hybrids with enhanced catalytic activity and stability for the oxidative removal of benzene. *Environmental Science & Technology*, *53*, 5926−5935.

Liu, H., Lu, X., Li, M., Zhang, L., Pan, C., Zhang, R., Li, J., & Xiang, W. (2018). Structural incorporation of manganese into goethite and its enhancement of Pb(II) adsorption. *Environmental Science & Technology*, *52*, 4719−4727.

Liu, L., Li, J., Zhang, H., Li, L., Zhou, P., Meng, X., Guo, M., Jia, J., & Sun, T. (2019). In situ fabrication of highly active γ-MnO_2/$SmMnO_3$ catalyst for deep catalytic oxidation of gaseous benzene, ethylbenzene, toluene, and o-xylene. *Journal of Hazardous Materials*, *362*, 178−186.

Liu, L., Shen, B., Lu, F., & Peng, X. (2023). Highly efficient Mn-Fe bimetallic oxides for simultaneous oxidation of NO and toluene: performance and mechanism. *Fuel*, *332*, 126143−126157.

Liu, Y., Zhang, T., Li, S., Zhang, K., Wang, X., Zhan, Y., Zheng, Y., & Jiang, L. (2020). Geometric and electronic modification of the active Fe^{3+} sites of α-Fe_2O_3 for highly efficient toluene combustion. *Journal of Hazardous Materials*, *398*, 123233−1232342.

Liu, Z., Zhang, Y., Jiang, S., Liu, S., Cao, J., & Ai, Y. (2022). Enhanced catalytic performance and reduced by-products emission on plasma catalytic

oxidation of high-concentration toluene using Mn-Fe/rGo catalysts. *Journal of Environmental Chemical Engineering*, *10*, 108770−108778.

Mane, R., Kim, H., Han, K., Kim, K.-J., Soo Lee, S., Roh, H.-S., Lee, C., & Jeon, Y. (2023). Pivotal role of MnO_x physicochemical structure in soot oxidation activity. *Fuel*, *346*, 1282870−128298.

Mansoori, A.M., Ando, N., & Higuchi, T. (2019). Influence of phosphorus and trace metals in biofilters treating gaseous VOCs using a novel irrigation system. *Journal of the Air & Waste Management Association*, *69*, 1348−1360.

Miao, C., Chen, S., Liang, L., Shang, K., & Ouyang, J. (2023). Construction of flower spherical Cr–Ce/ZSM-5 catalyst with rich surface structure and study on CO_2-assisted ethane dehydrogenation performance. *Microporous and Mesoporous Materials*, *348*, 112392–112401.

Miao, C., Chen, S., Shang, K., Liang, L., & Ouyang, J. (2022). Highly active Ni–Ru bimetallic catalyst integrated with MFI Zeolite-loaded cerium zirconium oxide for dry reforming of methane. *ACS Applied Materials & Interfaces*, *14*, 47616–47632.

Mo, S., Zhang, Q., Li, J., Sun, Y., Ren, Q., Zou, S., Zhang, Q., Lu, J., Fu, M., Mo, D., Wu, J., Huang, H., & Ye, D. (2020). Highly efficient mesoporous MnO_2 catalysts for the total toluene oxidation: oxygen-vacancy defect engineering and involved intermediates using in situ drifts. *Applied Catalysis B: Environmental*, *264*, 118464–118479.

Nie, L., Mei, D., Xiong, H., Peng, B., Ren, Z., Hernandez, X.I.P., DeLaRiva, A., Wang, M., Engelhard, M.H., Kovarik, L., Datye, A.K., & Wang, Y. (2017). Activation of surface lattice oxygen in single-atom $PtCeO_2$ for low-temperature CO oxidation. *Science*, *358*, 1419–1423.

Oh, S.J., Cook, D.C., & Townsend, H.E. (1998). Characterization of iron oxides commonly formed as corrosion products on steel. *Hyperfine Interactions*, *112*, 59–66.

Patterson, T.A., Carver, J.C., Leyden, D.E., & Hercules, D.M. (1976). A surface study of cobalt-molybdena-alumina catalysts using X-ray photoelectron spectroscopy. *Journal of Physical Chemistry*, *80*, 1700–1708.

Pöschl, U., & Shiraiwa, M. (2015). Multiphase chemistry at the atmosphere–biosphere interface iinfluencing climate and public health in the Anthropocene. *Chemical Reviews*, *115*, 4440–4475.

Qin, L., Huang, X., Zhao, B., Wang, Y., & Han, J. (2019). Iron oxide as a promoter for toluene catalytic oxidation over Fe–Mn/γ-Al_2O_3 catalysts. *Catalysis Letters*, *150*, 802–814.

Ranjbaran, F., Kamio, E., & Matsuyama, H. (2018). Toluene vapor removal using an inorganic/organic double-network ion gel membrane. *Separation Science and Technology*, *53*, 2840–2851.

Rastegarpanah, A., Deng, J., Liu, Y., Jing, L., Pei, W., Wang, J., & Dai, H. (2023). Bamboo-like MnO_2·Co_3O_4: high-performance catalysts for the oxidative removal of toluene. *Journal of Environmental Sciences*, *147*, 617–629.

Rezaei, P., Rezaei, M., & Meshkani, F. (2019). Ultrasound-assisted hydrothermal method for the preparation of the M-Fe_2O_3-CuO (M: Mn, Ag, Co) mixed oxides nanocatalysts for low-temperature CO oxidation. *Ultrason Sonochem*, *57*, 212–222.

Rochard, G., Olivet, L., Tannous, M., Poupin, C., Siffert, S., & Cousin, R. (2021). Recent advances in the catalytic treatment of volatile organic compounds: a review based on the mixture effect. *Catalysts*, *11*, 1218–1238.

Rousseau, S., Loridant, S., Delichere, P., Boreave, A., Deloume, J.P., & Vernoux, P. (2009). $La_{(1-x)}Sr_xCo_{1-y}Fe_yO_3$ perovskites prepared by sol–gel method: characterization and relationships with catalytic properties for total oxidation of toluene. *Applied Catalysis B: Environmental*, *88*, 438–447.

Sahin, R., Tapadia, K., & Sharma, A. (2016). Kinetic and isotherm studies on adsorption of fluoride by limonite with batch technique. *Journal of Environmental Biology*, *37*, 919–926.

Saqer, S.M., Kondarides, D.I., & Verykios, X.E. (2011). Catalytic oxidation of toluene over binary mixtures of copper, manganese and cerium oxides supported on γ-Al_2O_3. *Applied Catalysis B: Environmental*, *103*, 275–286.

Shah, P.M., Bailey, L.A., Morgan, D.J., & Taylor, S.H. (2023). The effect of metal ratio and precipitation agent on highly active iron-manganese mixed metal oxide catalysts for propane total oxidation. Catalysts, *13*, 794–810.

Shen, Y., Deng, J., Han, L., Ren, W., & Zhang, D. (2022). Low-temperature combustion of toluene over Cu-doped $SmMn_2O_5$ mullite catalysts via creating highly active Cu^{2+}−O−Mn^{4+} sites. *Environmental Science & Technology*, *56*, 10433–10441.

Shen, Y., Deng, J., Hu, X., Chen, X., Yang, H., Cheng, D., & Zhang, D. (2023). Expediting toluene combustion by harmonizing the Ce−O strength over Co-doped CeZr oxide catalysts. *Environmental Science & Technology*, *57*, 1797–1806.

Spanier, J.E., Robinson, R.D., Zhang, F., Chan, S.-W., & Herman, I.P. (2001). Size-dependent properties of CeO_{2-y} nanoparticles as studied by Raman scattering. *Physical Review B*, *64*, 245407–245413.

Sun, Y., Xu, S., Bai, B., Li, L., Kang, Y., Hu, X., Liao, Z., & He, C. (2022). Biotemplate fabrication of hollow tubular $Ce_xSr_{1-x}TiO_3$ with regulable surface acidity and oxygen mobility for efficient destruction of chlorobenzene: intrinsic synergy effect and reaction mechanism. *Environmental Science & Technology*, *56*, 5796–5807.

Tang, J., Zhao, L., Jiang, S., Huang, Y., Zhang, J., & Li, J. (2022). Effect of transition-metal oxide M (M = Co, Fe, and Mn) modification on the performance and structure of porous CuZrCe catalysts for simultaneous removal of NO and toluene at low−medium temperatures *Energy & Fuels*, *36*, 4439–4455.

Thibeau, R.J., Brown, C.W., & Heidersbach, R.H. (1978). Raman spectra of possible corrosion products of iron. *Applied Spectroscopy*, *32*, 532–535.

Toda, K., Tanaka, T., Tsuda, Y., Ban, M., Koveke, E.P., Koinuma, M., & Ohira, S.-I. (2014). Sulfurized limonite as material for fast decomposition of organic compounds by heterogeneous fenton reaction. *Journal of Hazardous Materials*, *278*, 426–432.

Tsubouchi, N., Hashimoto, H., & Ohtsuka, Y. (2015). High catalytic performance of magnesium cations-added limonite in the decomposition of ammonia in a simulated syngas-rich fuel gas. *Journal of Molecular Catalysis A: Chemical*, *407*, 75–80.

Wang, P., Wang, J., An, X., Shi, J., Shangguan, W., Hao, X., Xu, G., Tang, B., Abudula, A., & Guan, G. (2021a). Generation of abundant defects in Mn-Co mixed oxides by a facile agar-gel method for highly efficient catalysis of total toluene oxidation. *Applied Catalysis B: Environmental*, *282*, 119560–119571.

Wang, Y., He, J., Li, X., Wang, M., Zhou, Y., Xiao, J., Chen, D., & Lu, J. (2021b). Low temperature combustion of VOCs with enhanced catalytic activity over MnO_2 nanotubes loaded with Pt and Ni–Fe spinel. *ACS Applied Materials & Interfaces*, *13*, 46830–46839.

Wang, Y., Zhang, L., & Guo, L. (2018). Enhanced toluene combustion over highly homogeneous iron manganese oxide nanocatalysts. *ACS Applied Nano Materials*, *1*, 1066–1075.

White, W.B., & Keramidas, V.G. (1972). Vibrational spectra of oxides with the c-type rare earth oxide structure. *Spectrochimica Acta Part A: Molecular Spectroscopy*, *28*, 501–509.

Xue, T., Li, R., Gao, Y., & Wang, Q. (2020). Iron mesh-supported vertically aligned Co-Fe layered double oxide as a novel monolithic catalyst for catalytic oxidation of toluene. *Chemical Engineering Journal*, *384*, 123284–123294.

Yadav, M., Pophali, A., Verma, N., & Kim, T. (2022). Oxidation of VOCs on a highly stabilized furfuryl alcohol-based activated carbon supported nickel oxide catalyst. *Journal of Industrial and Engineering Chemistry*, *105*, 313–323.

Yan, X., Shao, J., Wen, Q., & Shen, J. (2020). Stabilization of soil arsenic by natural limonite after mechanical activation and the associated mechanisms. *Science of the Total Environment*, *708*, 135118–135124.

Yang, W., Su, Z.a., Xu, Z., Yang, W., Peng, Y., & Li, J. (2020). Comparative study of α-, β-, γ- and δ-MnO_2 on toluene oxidation: oxygen vacancies and reaction intermediates. *Applied Catalysis B: Environmental*, *260*, 118150–118159.

Zhang, C., Chen, T., Liu, H., Chen, D., Xu, B., & Qing, C. (2018). Low temperature SCR reaction over nano-structured Fe-Mn oxides: characterization, performance, and kinetic study. *Applied Surface Science*, *457*, 1116–1125.

Zhang, J., Zou, J., Xu, X., Li, Z., Zeng, Z., & Li, L. (2022). Nitrogen-doped porous carbon from biomass with efficient toluene adsorption and superior catalytic performance. *Materials*, *15*, 8115–8129.

Zhu, R., Zhou, Q., Zhu, J., Xi, Y., & He, H. (2015). Organo-clays as sorbents of hydrophobic organic contaminants: sorptive characteristics and approaches to enhancing sorption capacity. *Clays and Clay Minerals*, *63*, 199–221.

https://doi.org/10.1017/cmn.2024.19 Published online by Cambridge University Press